Binary Kinetics in the Y–Ba–Cu System: 2. Nanosized Particles

Hong Wang and William J. Thomson
Dept. of Chemical Engineering, Washington State University, Pullman, WA 99164

The kinetics of binary mixtures of $Y_2O_3-BaCO_3(Y-Ba)$, $BaCO_3-CuO(Ba-Cu)$ and $Y_2O_3-CuO(Y-Cu)$ prepared by citrate sol–gel techniques were studied in both air and helium. Particle sizes resulting from the sol–gel preparation were between 5 and 100 nm, and the prevailing kinetics differed significantly from those observed in the companion study of micron-sized particles. That is, nucleation-growth kinetics of the Avrami–Erofe'ev type adequately model the kinetics over the entire conversion range as opposed to the diffusion mechanisms that describe the kinetics in larger sized particles. An alternate nucleation-growth model, which neglects overlapping volumes during reaction (Austin–Rickett model), was also adequate in the Ba–Cu system where particle size/spacing was larger, but was only applicable in other reaction systems at lower conversions. Activation energies obtained from the Avrami–Erofe'ev were consistently lower than those from the Austin–Rickett model, because the former model contains two parameters that are temperature-sensitive.

Introduction

Recent advances in the large-scale synthesis of nanosized powders have implications relative to the design of processing units to produce materials derived from these powders. One such implication is that a knowledge of the kinetics associated with materials production will be of increasing importance. In the first part of this study, Sobolik and Thomson (1995) have described an experimental technique, dynamic X-ray diffraction (DXRD), which provides experimental measurements necessary for kinetic studies of solid–solid reactions, and have pointed to the lack of kinetic information relative to the formation of the "123," Y–Ba–Cu high-temperature superconductor $YBa_2Cu_3O_x$ $(6 \le x \le 7)$. In their study, which concentrated on particle sizes in the micrometer range, the kinetics were found to be dependent on the reaction rates at solid–solid interfaces as well as on solid-state diffusion through product layers. Nanosized materials, however, are far more reactive and, typically, nucleation/growth phenomena are the controlling factors (Avrami, 1939, 1940, 1941).

Although there has been some effort to elucidate the details of the phase diagrams for these mixtures (Wang et al., 1987; De Leeuw et al., 1988; and Hinks et al., 1987), virtually all of the reaction kinetics studies have utilized relatively large particles (micron-sized) and the observed reaction rates were diffusion limited. Furthermore, it is known that smaller particles not only induce higher reaction rates, but can also lead to different reaction products. Using DXRD, and a systematic approach, Sobolik and Thomson were able to determine the slowest reaction step among the three binary pairs of micro-sized particles and to successfully model their results using accepted diffusion-limited rate models. Here we present a similar study using identical techniques, but utilizing nanometer-sized particles derived from citrate sol–gel techniques.

Correspondence concerning this article should be addressed to W. J. Thomson.

Theoretical Considerations

Since it is likely that nucleation and growth phenomena will govern the reaction rates, at least during the initial stage of the reactions (Sobolik et al., 1994), it is useful to review the theoretical development of rate expressions based on such models.

The nucleation and growth mechanisms developed by Avrami (1939, 1940, 1941) and Erofe'ev (1946) can be used to describe either a heterogeneous reaction or a phase transformation. In such reactions, a new phase is nucleated by germ

Table 1. Kinetic Models for Solid-State Reactions

Rate Controlling Mechanism	$F(\alpha)=\int_0^\alpha d\alpha/df(\alpha)$	$f(\alpha)$	x
Zero order	α	1	t
First order	$-\ln(1-\alpha)$	$(1-\alpha)^{-1}$	t
1-D diffusion	α^2	$(2\alpha)^{-1}$	t
2-D diffusion	$(1-\alpha)\ln(1-\alpha)+\alpha$	$[-\ln(1-\alpha)]^{-1}$	t
Diff. (Jander)	$[1-(1-\alpha)^{1/3}]^2$	$3/2(1-\alpha)[1-(1-\alpha)^{1/3}]^{-1}$	t
Diff. (Ginstling and Brounshtein)	$(1-2\alpha/3)-(1-\alpha)^{2/3}$	$3/2[(1-\alpha)^{1/3}-1]^{-1}$	t
Diff. (Carter)	$(1+\alpha)^{2/3}+(1-\alpha)^{2/3}$	$3/2[(1+\alpha)^{-1/3}-(1-\alpha)^{-1/3}]^{-1}$	t
Phase boundary (disk)	$1-(1-\alpha)^{1/2}$	$2(1-\alpha)^{1/2}$	t
Phase boundary (sphere)	$1-(1-\alpha)^{1/3}$	$3(1-\alpha)^{2/3}$	t
Nucl. (1-D Avrami-Erofe'ev)	$[-\ln(1-\alpha)]^{1/3}$	$2(1-\alpha)[-\ln(1-\alpha)]^{1/2}$	t
Nucl. (2-D Avrami-Erofe'ev)	$[-\ln(1-\alpha)]^{1/2}$	$3(1-\alpha)[-\ln(1-\alpha)]^{2/3}$	t
Nucl. (general Avrami-Erofe'ev)	$\ln\ln[1/(1-\alpha)]$	$-(1-\alpha)\ln(1-\alpha)$	$\ln t$
Austin-Rickett	$\ln[\alpha/(1-\alpha)]$	$\alpha(1-\alpha)$	$\ln t$
Prout-Tompkins	$\ln[\alpha/(1-\alpha)]$	$\alpha(1-\alpha)$	t

nuclei contained in the old phase and could be reactants or foreign particles. The new phase can then grow through activation and become a grain/particle once the size is larger than the critical size needed for the growth. For example, Burgers and Groen (1957) studied the phase transformation of tin and found that the transformation from gray to white tin followed the Avrami–Erofe'ev nucleation mechanism. Hulbert and Klawitter (1967) studied the reaction between zinc oxide (particle sizes 0.1–1.0 μm) and barium carbonate (particle sizes 0.1–3.0 μm) and found that the reaction rate could also be described by the general Avrami–Erofe'ev nucleation mechanism.

In general, solid-state reactions can be controlled by (a) diffusion-controlled reactions; (b) processes occurring at interfaces, that is, phase boundary-controlled reactions; and (c) nucleation and growth-controlled reactions. The mathematics describing the different reaction rate controlling mechanisms are summarized in Table 1. In all of these mechanisms, the conversion α (the fraction of product formed or reactant consumed) is related to the time t under isothermal conditions. The kinetics of these mechanisms can generally be expressed in differential form as

$$\frac{d\alpha}{dX}=kf(\alpha) \tag{1}$$

where X is either t or $\ln(t)$ and k is a value that depends on the shape of the nucleus and the number of electrons necessary for the formation of a stable nucleus. In integral form, Eq. 1 can be expressed as

$$\int_0^\alpha \frac{d\alpha}{f(\alpha)}=\int_{X_0}^{X} k\,dX \tag{2}$$

or, after integration, as

$$F(\alpha)=kX+C \tag{3}$$

where X_0 is the initial condition corresponding to $\alpha=0$, C is a constant, and $F(\alpha)=\int_0^\alpha[d\alpha/f(\alpha)]$. The particular form of $F(\alpha)$ depends on the specified rate controlling mechanism, as listed in Table 1.

Based upon the theory of nucleation and growth mechanisms for a heterogeneous reaction or a phase transformation, as developed by Avrami (1939, 1940, 1941) and Erofe'ev (1946) in the 1940s, Eq. 3 takes on the form

$$\ln\ln\left(\frac{1}{1-\alpha}\right)=k\ln t+\ln B \tag{4}$$

where B is related to the nucleation rate by

$$B=\sigma G^a N_0 n. \tag{5}$$

In Eq. 5, σ is determined by the shape of the nuclei, G is the linear growth rate from a growth nucleus, N_0 is the initial number of nuclei, and n is the formation probability of growth nuclei. For linear growth processes, k varies with temperature, n, and the shape of growth nuclei. According to Eq. 4, both B and k can be determined at any given temperature by plotting $\ln\ln[1/(1-\alpha)]$ vs. $\ln(t)$, where the slope is k and the intercept is $\ln(B)$. Since new phase growth is an activated process, we can rearrange Eq. 4 and then differentiate it so that it is in a form more typical of kinetic rate expressions, namely,

$$\frac{d\alpha}{dt}=kBt^{k-1}(1-\alpha). \tag{6}$$

Since both k and B vary with temperature, we can take the product, kB, to vary in an Arrhenius manner so that

$$kB=A\exp\left[-\frac{E}{RT}\right]. \tag{7}$$

Therefore, the activation energy can be obtained by plotting $\ln kB$ vs. $1/T$ and finding the slope.

Under conditions where the reaction is isothermal, the new phase is typically very finely grained (Avrami, 1940), and the overlapping of the transformed volume is sufficiently small that it can be ignored. In this case, Austin and Rickett (1938) empirically determined the following special case of the Avrami–Erofe'ev nucleation and growth mechanism

$$\ln\left(\frac{\alpha}{1-\alpha}\right) = k \ln t + \ln B \tag{10}$$

where B is a function of temperature only and k is a constant. This rate expression has a differential form of

$$\frac{d\alpha}{dt} = Bt^{k-1}(1-\alpha)^2, \tag{11}$$

and consequently we expect that, at each temperature, a plot of

$$\ln\left(\frac{\alpha}{1-\alpha}\right)$$

vs. $\ln t$ should yield straight lines of constant slope k and intercept $\ln B$. On this basis, B should be dependent on T in an Arrhenius manner, that is,

$$B = B_0 \exp\left[-\frac{E}{RT}\right]. \tag{12}$$

In this study, the reaction rates of the three binary combinations of the precursors to the 123 high-temperature superconductor, $BaCO_3/CuO$, $Y_2O_3/BaCO_3$, and Y_2O_3/CuO, were determined when the binary mixtures were prepared from citrate sol-gels (Pechini, 1963). The experiments were conducted in both air and helium environments, and the ratio of metal elements for all three mixtures was Y:2Ba:3Cu, the same as in the 123 high-temperature superconductor, $Y_1Ba_2Cu_3O_x$ $(6 \le x \le 7)$. The conversion data were then placed into the form of Eq. 3 and evaluated as to their compatibility with the reaction mechanisms listed in Table 1. The activation energies for the reaction of each mixture in both air and helium environments were then calculated from the temperature dependency of the conversion-time data resulting from a series of isothermal experiments on each binary system.

Experimental Studies

The citrate sol-gels were based on the Pechini method (Pechini, 1963) using citric acid, ethylene glycol, and the metals as metal oxides or carbonate. A mixture of citric acid and ethylene glycol was first heated to about 438 K to achieve cross-linked structures. This mixture was then diluted with water, and two of the three compounds (Y_2O_3, CuO, and $BaCO_3$) were added with the desired stoichiometry. After the mixture had been heated to remove excess solvent, the samples were dried in air at room temperature for 3–4 weeks to produce a transparent gel. Powder samples were obtained by a "burnout" procedure that involved repetitive heating in air to 873 K, interspersed with regrinding. This was done at least three times with a typical total burnout time of about 10 minutes.

DXRD (time/temperature resolved) (Thomson, 1989) was used to monitor crystal structure changes in the binary samples. The DXRD apparatus was utilized in the same manner as described in Part I of this study (Sobolik and Thomson, 1995) except that the lower reaction temperatures associated with the small particles sizes allowed for the use of an inconel rather than a Pt heating strip and the gas flow-through rate was lower (120 mL/min). The samples were rapidly heated to the desired temperature (typically in about 30 s) and then held at that temperature in either air or helium environments for continuous X-ray diffraction (XRD) scans. A set of isothermal experiments was typically carried out at five different temperatures for each binary mixture. The internal standard method (Cullity, 1978) using $BaZrO_3$ as the internal standard was employed to obtain mole fractions of the crystalline species present as a function of time. A Hitachi 600 transmission electron microscope (TEM) was employed to characterize the particle sizes of the starting materials. Typical TEM preparation methods were employed: samples were mixed with water, placed on a copper grid, and then dried under a lamp prior to the TEM scans.

Results and Discussion

The TEM images are shown in Figure 1 and are typical of all these powder samples. For the Y–Ba binary, the particle sizes range from 5 to 25 nm (average value of 7 nm), and from 5 to 35 nm (average value of 10 nm) for the Y–Cu mixture. The Ba–Cu binary mixture had the largest particle size, ranging from 55 to 190 nm with an average value of 120 nm. Qualitative elemental scans of the TEM images all indicated that both binary metallic elements were always present in the observed particles.

The isothermal experiments were extremely sensitive to the temperature under which the experiments were performed; even a small variation in temperature (± 5 K) could result in very different results, as shown in Figure 2. Since the limitations of the temperature controller made it very difficult to repeat isothermal experiments to this degree of precision, the isothermal experiments were conducted at the actual isothermal temperature achieved after the rapid heatup. In order to demonstrate that the measured data are reproducible, three nonisothermal reactions under identical conditions were performed by heating the sample at 5 K/min from 873 K to the temperature at which the reactions were complete. Conversion as a function of temperature for three of the duplicate nonisothermal experiments is shown in Figure 3 for the Ba–Cu system in air and, as can be seen, the results are very reproducible.

Figure 4 shows typical isothermal results for conversion as a function of time for all three mixtures in an air environment. The different temperatures for each mixture reflect the different reactivities of the binaries. In air there was only one product for each reaction; specifically,

$$BaCO_3 + CuO = BaCuO_2 + CO_2 \tag{R1}$$

$$Y_2O_3 + 4BaCO_3 = Ba_4Y_2O_7 + CO_2 \tag{R2}$$

$$Y_2O_3 + 2CuO = Y_2Cu_2O_5 \tag{R3}$$

Note that the conversions in Figure 4 are based on the limiting reactants except in the case of the Y–Cu system, where it is based on $Y_2Cu_2O_5$ since this was a more accurate XRD peak. In all cases the quantities of each reactant and product for all reactions were individually calculated, and the mass balances were in good agreement with the stoichiometry of

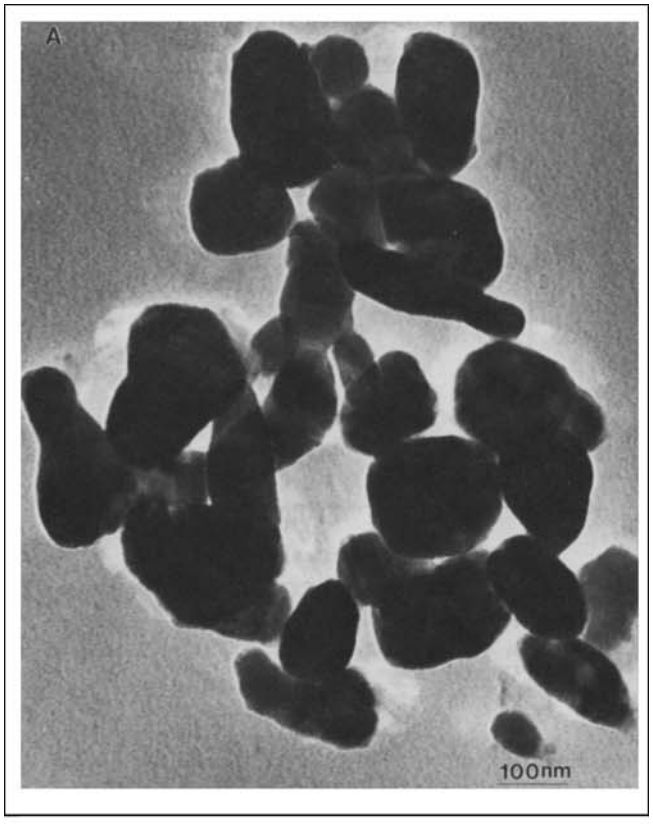

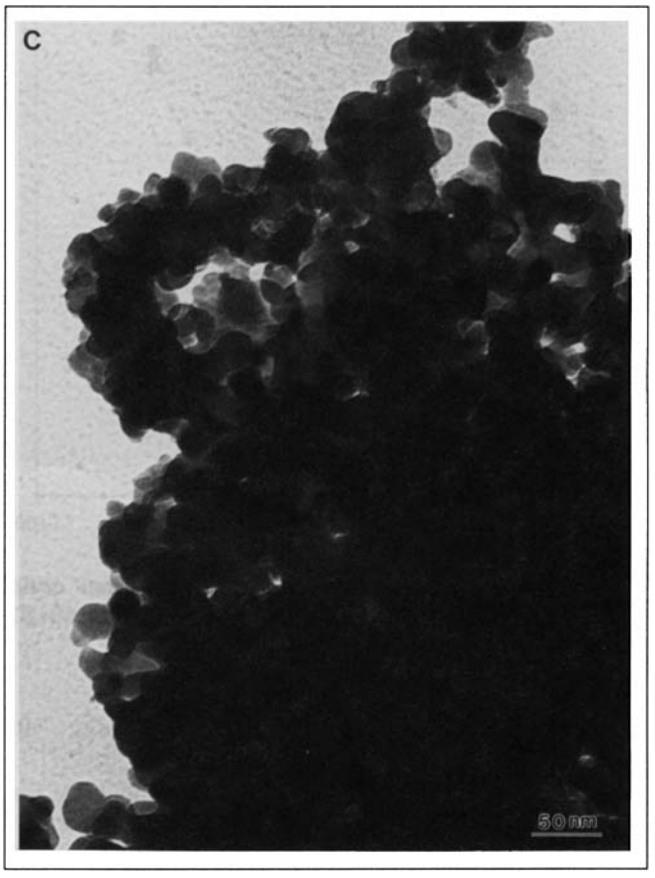

Figure 1. TEM images.

(a) $BaCO_3/CuO$; (b) $Y_2O_3/BaCO_3$; (c) Y_2O_3/CuO.

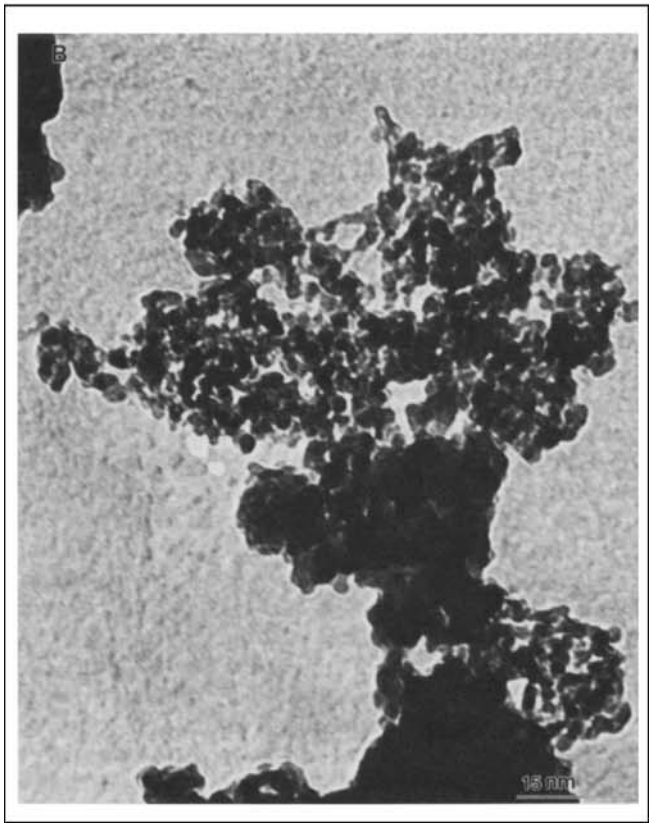

the reaction equations shown in Eqs. R1–R4. When these same reactions were carried out in a helium environment, the product for the Y–Ba system was also $Y_2Ba_4O_7$, but in the Ba–Cu system, the following reaction took place

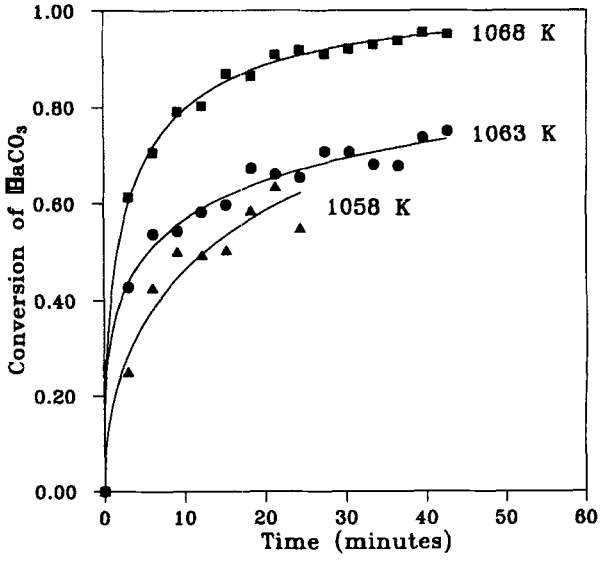

Figure 2. Example of temperature sensitivity ($BaCO_3(\alpha)$–CuO in air).

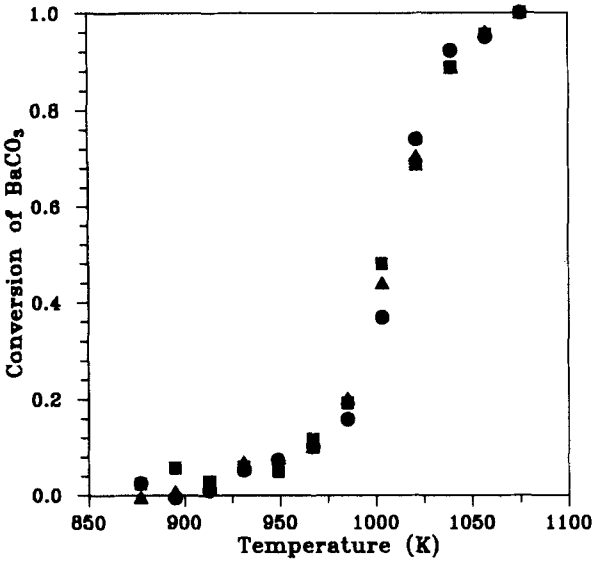

Figure 3. Reproducibility under nonisothermal conditions ($BaCO_3(\alpha)$–CuO system in air, from 873 K at 5 K/min).

$$BaCO_3 + 2CuO = BaCu_2O_2 + CO_2 + (1/2)O_2 \quad (R4)$$

When the Y–Cu binary was heated in helium, multiple reactions occurred and thus kinetic analyses of the type shown in Table 1 could not be carried out over a wide temperature range. This reaction system is addressed in more detail at the end of the article.

In all cases, the conversion curves rise rapidly and then level off (as in Figure 4), a characteristic of nucleation-growth phenomena (Avrami, 1939). In order to evaluate compatability with the appropriate reaction mechanisms, conversion data for each reaction were fitted for all the kinetic models listed in Table 1 by plotting $F(\alpha)$ against X and then examining

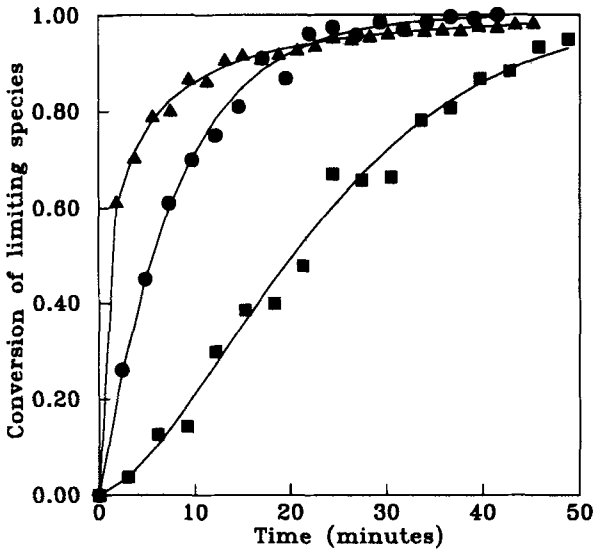

Figure 4. Conversions in air.

▲ = $BaCO_3(\alpha)$ in Ba–Cu at 1,068 K; ● = $BaCO_3(\beta)$ in Y–Ba at 1,143 K; ■ = $Y_2Cu_2O_5$ in Y–Cu at 1,043 K.

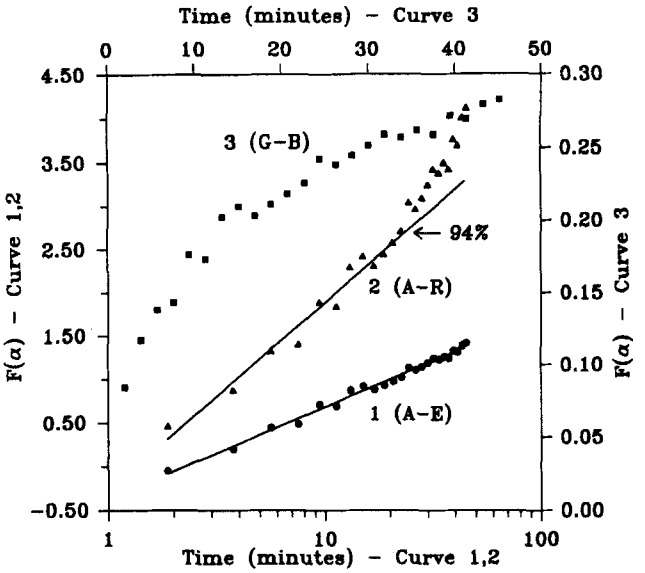

Figure 5. $F(\alpha)$ vs. ln(t): $BaCO_3(\alpha)$–CuO in air at 1,068 K.

A–E = Avrami-Erofe'ev; A–R = Austin–Rickett; G–B = Ginstling–Brounshtein.

the linearity of the plots. We found that only the Avrami–Erofe'ev (A–E) and the Austin–Rickett (A–R) nucleation models were able to fit the data over reasonable ranges of conversion. Given the shapes of the conversion curves in Figure 4, it is not surprising to find that only the mechanisms in Table 1 with $X = \ln t$ give reasonable fits. In the following discussion, we will limit ourselves to only these two mechanisms.

A test of the linearity of plots of $F(\alpha)$ vs. ln (t) for the reaction between $BaCO_3$ and CuO in air are shown as an example in Figure 5. In addition to the A–E and A–R models, an evaluation of the Ginstling–Brounshtein (G–B) diffusion model (Ginstling and Brounshtein, 1950) is also shown. As can be seen, a straight line provides an excellent fit for both the A–E and the A–R nucleation models, to conversions of 98% and 94%, respectively. On the other hand, when the data are applied to the Ginstling–Brounshtein model, the data do not fit the model over any reasonable range of conversion. Since the latter model was successfully used by Sobolik and Thomson (1995) to model the kinetics for 5–45 μm particles of this same reaction system, it points to the significance of particle size in modeling the kinetics of these reactions. It is clear from Figure 5 that either the A–E or the A–R model is compatible with the Ba–Cu kinetic data. While all the other four reactions showed similar results, namely, that the A–E model fit the data over the entire conversion range, the A–R model was only able to fit the data up to certain conversions. Table 2 shows the highest conversion at which the A–R model fits the data (at the highest temperatures employed in each system) and ranges from 94% in the Ba–Cu (air) system (1,068 K) to as low as 60% in the Y–Ba (air) system (1,183 K). A possible explanation for the fact that the A–R model consistently fails to fit the data at high conversions is that this mechanism ignores the overlapping volume of transformed matter during the growth of particles. This is a valid assumption only up to conversion values where

Table 2. Upper Conversion Limits for Applicability of A–R Model

Reaction System	Conversion Limit (α)	
	Air	Helium
Ba–Cu	0.94	93
Y–Ba	0.60	0.75
Y–Cu	0.75	–

the overlapping effect is small. When the conversion get large, however, the overlapping of the volume of transformed matter can be significant. As indicated in Table 2, the A–R model can be applied to the Ba–Cu system in both air and helium environments, up to 94% conversion, the highest conversion of all of the investigated reaction systems. This result is also consistent with the neglect of the overlapping volumes during reaction. That is, referring to the TEM images of the initial Ba–Cu mixture (Figure 1a) it can be seen that, due to the large particle sizes in this mixture (on the order of 100 nm), the particle spacing is also much larger than in the other two binary systems. Therefore, in the Ba–Cu system there is more room for particles to grow individually, and volume overlapping could easily be negligible until conversions become very high. Thus the A–E model appears to be the model of choice for all three binary reaction systems, and examples of how well this model fit the conversion data can be gleaned by comparing the model-derived curves with the experimental data points in Figures 2 and 4.

Individual values of B and k were calculated from the isothermal data, and the activation energies for these reactions were obtained from corresponding Arrhenius plots, using Eqs. 7 and 12 for the A–E and A–R models, respectively. As mentioned earlier, each isothermal experiment was carried out in a carefully chosen temperature zone so that the reaction would proceed at a reasonable rate, but not so fast that sufficient DXRD data could not be obtained. This temperature range was rather narrow, ranging from 883 to 983 K for the Ba–Cu system reaction in helium to as small as 1,123–1,183 K for the Y–Ba system reaction in air. Figure 6 shows typical Arrhenius plots for the A–E and A–R models,

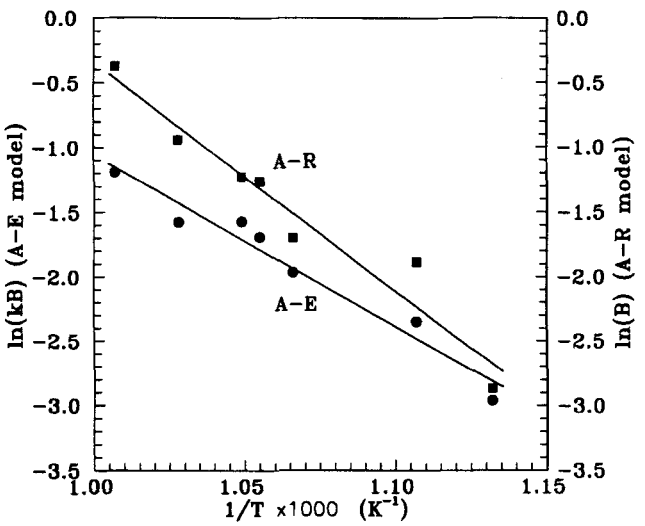

Figure 6. Arrhenius plots: A–E and A–R models ($BaCO_3$–CuO in helium).

Table 3. Activation Energies: A–E and A–R Models

Reaction System	Reaction Environ.	E(A–E) (kJ/mol)	E(A–R) (kJ/mol)	$E(k)$ (kJ/mol)	Temp. Range (K)
Ba–Cu	Air	151	255	–109	973–1,053
	Helium	111	145	–14	883–983
Y–Ba	Air	772	1,157	–173	1,113–1,183
	Helium	773	848*	–6	1,123–1,173
Y–Cu	Air	152	483	–206	993–1,083

*Based on the disappearance of β-$BaCO_3$.

in this case for the Ba–Cu reaction system in helium. As can be seen, the data form reasonable straight lines for both models, and this type of fit was typical for all five reactions.

The values of the activation energies and the isothermal temperature ranges used in the experiments are all listed in Table 3 for the three reaction systems. The narrow temperature ranges over which these data were collected, less than 100 K, is a consequence of the high activation energies listed in Table 3. It is interesting that the A–R model gives consistently higher activation energies than the A–E model. This is attributed to the fact that both k and B vary with temperature in the A–E model and, in fact, the specific form of the temperature dependency of k was found to vary substantially with the particular binary system as well as with the surrounding gas environment. In addition, the dependency of k on temperature was, in all cases, an *inverse* dependency. For example, in those systems where the differences in the activation energies between the A–E and A–R models were the greatest, the inverse temperature dependency of k is also the greatest, as can be seen from the *apparent* activation energy, $E(k)$, in Table 3. Again, this was another consequence of accounting for volume overlapping in the A–E model.

While there is little significant difference in the activation energies between the air and helium environments in the A–E model, the activation energies appear to be significantly lower in helium when using the A–R model. Again, the entire temperature dependency in the A–R model must be accounted for by the parameter B, and thus there is a wider variation here. The fact that it is higher in air than in helium is probably due to the influence of the CO_2 concentration in the air, which increases the reverse reaction rates of $BaCO_3$ and typically results in higher activation energies (Stern and Weise, 1969). Finally, consistent with its higher reaction temperatures, the Y–Ba system has much higher activation energies than the other two systems in both air and helium.

With the Y–Ba system in air, $BaCO_3$ first undergoes an $\alpha \rightarrow \beta$ phase transformation (beginning at 1,083 K) before reacting with Y_2O_3. In a helium environment, however, the reaction temperatures are lower and the transformation occurs simultaneously as it reacts with Y_2O_3. This is clearly shown in Figure 7 where the presence of both $BaCO_3$ phases is concurrent with the formation of the $Y_2Ba_4O_7$ product when the isothermal temperatures are below 1,123 K. Since we have previously observed that both the α and β phases of $BaCO_3$ will react with Y_2O_3 to form the $Y_2Ba_4O_7$ product (Sobolik et al., 1993), there are three simultaneous reactions here: the reactions of α– and β–$BaCO_3$ with Y_2O_3 as well

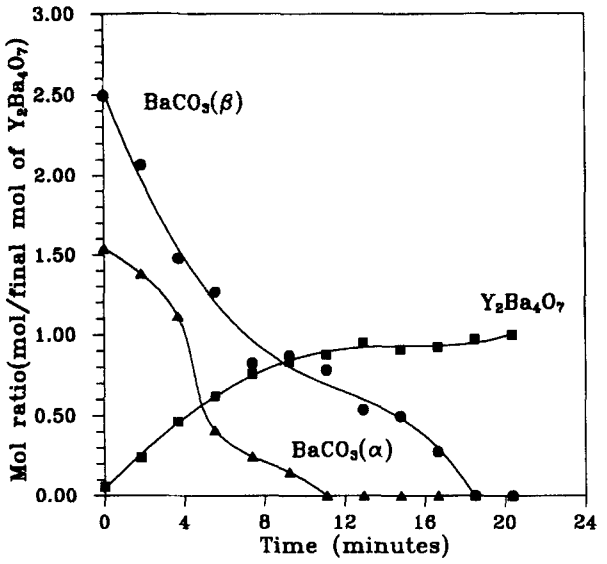

Figure 7. Phase changes in the Y-Ba system (1,088 K, helium).

as the $\alpha \rightarrow \beta$ phase transformation of $BaCO_3$. Consequently, in order to have a consistent basis for comparison between air and helium, the activation energies shown in Table 3 for the Y–Ba system were based on the disappearance of β–$BaCO_3$. Thus, in the helium environment, only temperatures above 1,123 K were used to calculate the activation energy (Table 3).

As mentioned earlier, the reactions between Y_2O_3 and CuO in a helium environment were considerably more complex due to the occurrence of simultaneous reactions that produced more than one product. In our earlier study of reaction paths (Sobolik et al., 1994), the binary products, $Y_2Cu_2O_5$ and $YCuO_2$, as well as Cu_2O were observed under nonisothermal conditions as the temperature was raised between 950 and 1,150 K. In this study we attempted to study the kinetics of these reactions by conducting isothermal experiments at relatively low temperatures so as to isolate the various reactions. Figure 8 shows the molar ratios of both initial reactants and the three products at a temperature of 923 K in helium. As can be seen, initially reaction R3 takes place, the same reaction observed in air. At about 60 min reaction time, CuO is then rapidly reduced to Cu_2O and is closely followed by the appearance of $YCuO_2$. The reduction of CuO is consistent with previous results (Sobolik et al., 1993), but the constancy of $Y_2Cu_2O_5$ is not. Since $Y_2Cu_2O_5$ was observed to reach a maximum concentration under nonisothermal conditions at higher temperatures, it appears that $Y_2Cu_2O_5$ does not decompose at these lower temperatures. Rather, two separate reactions take place:

$$Y_2O_3 + CuO = Y_2Cu_2O_5 \qquad (R3)$$

$$Y_2O_3 + Cu_2O = YCuO_2 \qquad (R5)$$

This result affords us the opportunity of obtaining kinetic data for both reactions R3 and R5. When the models listed in Table 1 were applied to Eq. R3, it was found that the A–E and A–R nucleation-growth models gave fits that were equally as good as any of the diffusion models (Jander, Ginstling, Carter). Undoubtedly, this is due to the relatively low conversions that were achieved (~ 30%, based on Y_2O_3). Figure 9 shows the test of linearity for the A–E and A–R models for reaction R5 and, in spite of the data scatter (attributed to the low concentrations), a reasonably good fit is achieved. In this case none of the diffusion models was able to fit the data. We conclude from this that the sudden appearance of Cu_2O results in a near instantaneous formation of numerous nuclei, and the reaction rate is likely governed by the growth of the $YCuO_2$ product. Again, the applicability of both the A–E and A–R models is due to the fact that the conversions are low so that the neglect of overlapping volumes is a good assumption.

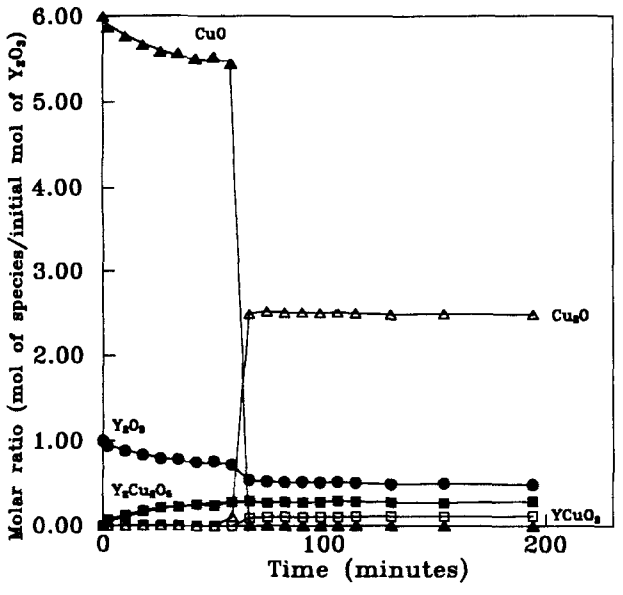

Figure 8. Y_2O_3–CuO system in helium (923 K).

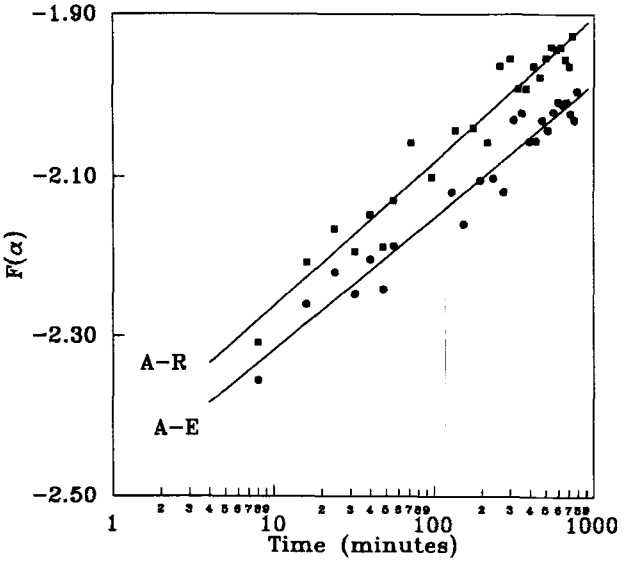

Figure 9. $F(\alpha)$ vs. ln(t): Reaction R5 in helium at 923 K.

A–E = Avrami-Erofe'ev; A–R = Austin–Rickett.

Conclusions

Based on these results, it is clear that the kinetics of nanosized particles in the Y–Ba and Ba–Cu systems in both air and helium as well as the Y–Cu system in air can be described by using models based on the nucleation mechanisms of the Avrami–Erofe'ev and Austin–Rickett types. While the A–E model was found to be appropriate throughout the entire conversion range, the A–R model was found to apply only up to certain conversions ranging from as high as 94% in the Ba–Cu system to as low as 60% in the Y–Ba system. This is attributed to the failure of the A–R model to account for the overlapping of the reacted volume that becomes more important at higher conversions. The success of the A–R model in the Ba–Cu system is likely a result of the larger particles in this system, which would lead to larger void spaces between the particles. The activation energies obtained from the A–R model were consistently higher than those obtained from the A–E model, and this is a direct result of the fact that the parameter k varies inversely with temperature in the A–E model. The fact that the activation energies from the A–R model were higher in an air environment is attributed to the presence of CO_2 in the air, which exerts a significant influence on the reversible nature of these reactions. Finally, it has been possible to also model the complex reaction system associated with the Y–Cu system in helium, and it was found that nucleation models are also appropriate for the second reaction in the sequence that is attributed to a "burst" of nucleation sites resulting from the rapid reduction of CuO to Cu_2O.

Acknowledgments

We thank the Boeing Company for its partial support of this work. We also thank the Washington State University Electron Microscopy Center for their assistance.

Notation

A,a = constant
$f(\alpha)$ = value for possible mechanisms
R = gas constant, 8.314 J/kmol
T = isothermal reaction temperature

Literature Cited

Austin, J. B., and R. L. Rickett, "Kinetics of the Decomposition of Austinite at Constant Temperature," *Metals Technol., T.P.*, No. 964 (Sept. 1938).

Avrami, M., "Kinetics of Phase Change: I," *J. Chem. Phys.*, **7**, 1103 (1939).

Avrami, M., "Kinetics of Phase Change: II," *J. Chem. Phys.*, **8**, 212 (1940).

Avrami, M., "Kinetics of Phase Change: III," *J. Chem. Phys.*, **9**, 177 (1941).

Burgers, W. G., and L. J. Groen, "Mechanism and Kinetics of the Allotropic Transformation of Tin," *Discuss. Farad. Soc.*, **23**, 183 (1957).

Cullity, B. D., *Elements of X-Ray Diffraction*, 2nd ed., Addison-Wesley, Reading, MA (1978).

De Leeuw, D. M., C. A. H. A. Mutsaers, C. Langereis, H. C. A. Smoorenburg, and P. J. Pommers, "Compounds and Phase Compatibilities in the System Y_2O_3-BaO-CuO at 950°C," *Phisica C*, **152** 39 (1988).

Erofe'ev, B. V., "Generalized Equations of Chemical Kinetics and Its Application in Reactions Involving Solids," *C. R. Dokl. Acad. Sci. USSR*, **52**, 511 (1946).

Ginstling, A. M., and B. I. Brounshtein, "Diffusion Kinetics of Reactions in Spherical Particles," *Zh. Prikl. Khim. (Leningrad)*, **23**, 1249 (1950).

Hinks, D. G., L. Soderholm, D. W. Capone II, J. D. Jorgensen, I. K. Schuller, C. U. Segre, K. Zhang, and J. D. Grace, "Phase Diagram and Superconductivity in the Y-Ba-Cu-O System," *Appl. Phys. Lett.*, **50**, 1688 (1987).

Hulbert, S. F., and J. J. Klawitter, "Kinetics and Mechanism of the Reaction Between Zinc Oxide and Barium Carbonate," *J. Am. Ceram. Soc.*, **50**, 484 (1967).

Pechini, M. P., U.S. Patent 304-434 (Aug., 1963).

Sobolik, J. L., and W. J. Thomson, "Binary Kinetics in the Y-Ba-Cu System: I. Micrometer Particles," *AIChE J.*, **4**(6), 00 (1995).

Sobolik, J. L., H. Wang, and W. J. Thomson, "The Effect of Particle Size on Binary Reactions Common to the Y-Ba-Cu-O System," *J. Amer. Ceram. Soc.*, **7**, 2738 (1994).

Stern, K. H., and E. L. Weise, "High Temperature Properties and Decomposition of Inorganic Salts. Part 2, Carbonates," Nat. Stand. Ref. Data Ser., Nat. Bur. of Stds., Washington, DC (1969).

Thomson, W. J., "Dynamic X-ray Diffraction: A Technique for Following Solid-State Reactions," *Ceram. Trans.*, **5**, 131 (1989).

Wang, G., S.-J. Hwu, S. N. Song, J. B. Ketterson, L. D. Marks, K. R. Poeppelmeier, and T. O. Mason, "950°C Subsolidus Phase Diagram for Y_2O_3-BaO-CuO System in Air," *Adv. Ceram. Mat.*, **2**, Special Issue, 313 (1987).

Manuscript received Jan. 18, 1994, and revision received June 15, 1994.